electronics

MDPI

Article

A Self-Decoupled Dual-Band MIMO Antenna for UAV Applications

Yiming Huang, Yu Lu, Jun Dong, Pu Ren, Yan Fang and Lingsheng Yang *

School of Electronic and Information Engineering, Nanjing University of Information Science and Technology, Nanjing 210044, China; 202383270578@nuist.edu.cn (Y.H.); lyu9836@163.com (Y.L.); 202412180593@nuist.edu.cn (J.D.); 202412492086@nuist.edu.cn (P.R.); 202512700923@nuist.edu.cn (Y.F.)
* Correspondence: ylsinchina@163.com

Abstract

To satisfy the demands of 5G communication and reliable data connectivity for unmanned aerial vehicles (UAVs), a novel two-element dual-band MIMO antenna with an inherent self-decoupling property based on orthogonal linear polarization diversity is proposed. Distinct from conventional designs relying on extra decoupling components, the antenna realizes isolation enhancement via coupled currents between annular strips and S-shaped strips without additional decoupling structures, representing the core design novelty. Fabricated on a low-cost 1.6 mm thick FR4 substrate, the antenna features compact overall dimensions of 60 mm × 30 mm × 1.6 mm, covering the 2.40–2.73 GHz ISM band and 3.38–3.63 GHz 5G Sub-6 GHz band. Measured results demonstrate that the reflection coefficient remains below −10 dB across the entire operating bands, with port isolation exceeding 27 dB for the 2.4 GHz band and 20 dB for the 3.5 GHz 5G band. The measured realized gain is 0.7–1.5 dB in the lower band and 2.3–2.9 dB in the upper band. The radiation efficiency, which is obtained exclusively from ANSYS HFSS 2025 R1 simulation, is higher than 90% for the lower band and over 80% for the upper band. The calculated envelope correlation coefficient (ECC) is less than 0.15 throughout the working bandwidth, which effectively suppresses inter-channel electromagnetic interference and mitigates channel fading caused by varying UAV attitudes to improve system channel capacity. Further verifications via epoxy encapsulation and co-simulation on an eight-rotor UAV platform prove slight frequency drift after packaging and installation, whereas its bandwidth and isolation still meet practical engineering requirements. Benefiting from a compact layout and omnidirectional radiation performance, the proposed low-cost MIMO antenna is convenient for conformal integration into a UAV fuselage, improving the practicability of UAV-aided emergency communication, equipment inspection and 5G network coverage.

Keywords: MIMO; UAV; dual-band antenna; self-isolation

Check for updates

Received: 23 May 2026
Revised: 12 June 2026
Accepted: 16 June 2026
Published: 24 June 2026

Copyright: © 2026 by the authors. Licensee MDPI, Basel, Switzerland. This article is an open access article distributed under the terms and conditions of the Creative Commons Attribution (CC BY) license.

1. Introduction

As 5G technology evolves toward dynamic, intelligent, and three-dimensional networks, unmanned aerial vehicles (UAVs), serving as aerial communication nodes, hold significant potential to expand network coverage and improve link capacity [1]. To simultaneously ensure flight control and high-bandwidth data transmission for UAVs, a dual-band cooperative antenna design is required. Specifically, the 2.4 GHz ISM band is used to ensure reliable links for flight control, telemetry, and image transmission between UAVs and ground stations [2] and can be extended to serve as an aerial Wi-Fi hotspot to

support multi-device access in emergency scenarios. For high-speed data transmission, the 3.38–3.63 GHz band is a sub-range of China's licensed 3300–3600 MHz 5G NR n78 spectrum, which follows the 3GPP Release 15 and Release 16 5G NR international standards and conforms to domestic radio management provisions for civil unmanned aerial vehicles. This band provides sufficient wideband resources to support UAV high-bandwidth services, including high-definition video backhaul, equipment inspection data transmission and emergency communication [3]. For small UAVs, limited payload capacity and strict aerodynamic requirements demand antennas with a low profile, light weight, conformal integration, and stable radiation performance [4,5].

To improve the data transmission efficiency and link reliability of UAVs in long-distance scenarios, antenna systems with wider operating bandwidths and higher radiation efficiency are essential.

Multiple-input multiple-output (MIMO) technology realizes parallel transmission of multiple data streams by deploying multi-antenna arrays at both the transmitter and receiver, thereby significantly enhancing channel capacity, spectrum efficiency, and link robustness without additional bandwidth or transmit power [6,7]. Integrating the MIMO architecture with a dual-band antenna design further exploits the synergistic advantages of frequency diversity and spatial diversity, effectively mitigating channel fading caused by UAV attitude variations and complex electromagnetic environments [8,9]. In addition, compact and lightweight MIMO antenna arrays can be designed as low-profile conformal structures to fit a UAV fuselage, meeting the stringent requirements of small UAVs for weight and aerodynamic shape and supporting applications demanding high throughput and reliability, such as high-definition video backhaul and swarm collaboration.

At present, researchers worldwide have proposed various MIMO antenna schemes for UAV applications [10]. For instance, a four-port circular wrench-shaped MIMO antenna array using defected ground structures was developed for UWB applications [11], and a dual-port microstrip MIMO antenna was designed for WLAN [12]. However, these designs do not cover the 2.4 GHz band and feature relatively high structural complexity. Various multi-band MIMO antenna solutions for UAVs have also been reported. Raza et al. [13] designed a four-port dual-band MIMO antenna array that suppresses mutual coupling through a four-element square rotational layout, achieving measured isolation of 23 dB and 19 dB at 2.4 GHz and 5.8 GHz, respectively. Nevertheless, the four-port configuration results in a large overall size, which is unfavorable for integration. Chao Zhang et al. [14] proposed a multi-band conformal MIMO antenna using four metamaterial units to cover 2.8 GHz, 5–7 GHz, and other bands, with isolation up to 54 dB realized via slotted rings and dumbbell-shaped structures. Yet its structure is complicated, the profile is high, and it does not include the 3.5 GHz 5G band. Akhter et al. [15] developed a dual-mode thin broadband MIMO antenna system with a triangular three-element layout, achieving bandwidths of 4% and 7% at 2.4 GHz and 5.2 GHz with a gain of approximately 10 dBi, but the 2.4 GHz bandwidth is narrow and 3.5 GHz operation is not supported. Tang et al. [16] developed a low-profile flexible dual-band quasi-isotropic antenna achieving quasi-isotropic radiation at 2.4 GHz and 4.6 GHz, and a 2×2 MIMO system was deployed on a UAV for field tests. However, its operating bands still lack coordination with 5G. In summary, existing schemes fail to simultaneously cover the important dual-band combination of 2.4 GHz (ISM/Wi-Fi) and 3.5 GHz (5G sub-6 GHz), and most adopt three-element or four-element configurations with high structural redundancy.

Distinct from previously reported UAV MIMO antennas that improve isolation by increasing element spacing, orthogonal layout, defected ground structures or dedicated additional decoupling branches, the proposed antenna realizes intrinsic self-decoupling by relying on orthogonal linear polarization diversity and the reverse induced coupling current

on S-shaped strips. Different from conventional independently designed decoupling structures that only serve coupling suppression, the S-shaped strips are an integral part of the radiating element. They not only participate in the construction of dual-band resonant modes and regulate the antenna impedance matching, but also induce reverse coupling currents to cancel the mutual coupling energy between elements, achieving the self-decoupling effect without introducing extra dedicated decoupling components. Benefiting from the self-isolation design, the antenna adopts only two radiators to realize dual-band coverage of 2.4 GHz ISM and 3.5 GHz Sub-6 GHz 5G, featuring a more compact electrical dimension and lower fabrication cost with an FR4 substrate. With a compact two-element layout, the antenna effectively suppresses mutual coupling between elements through reasonable array configuration and port optimization, achieving favorable isolation and omnidirectional radiation characteristics in dual bands. Comprehensive performance evaluation via electromagnetic simulation and prototype testing shows that the proposed MIMO antenna realizes dual-band operation while effectively improving channel capacity and spectrum efficiency, providing better transmission reliability and coverage flexibility for UAV communication systems. It is suitable for UAV applications such as emergency communications, inspection, and monitoring.

2. Antenna Design Procedure

In this paper, a MIMO antenna with a coplanar waveguide structure is designed. The antenna is fabricated on an FR4 substrate with a relative permittivity of 4.4, a loss tangent of 0.02, and a thickness of 1.6 mm. The proposed MIMO antenna system consists of two identical radiating elements. Each element is composed of a pair of coupled loop structures, a pair of S-shaped structures, and a ground portion. The distance between the two loop structures is denoted as D_1, and the distance between the two S-shaped structures is denoted as D_5.

As shown in Figure 1, the orange loop structure is formed by strips L_{11}, L_{12}, L_{21}, L_{22}, L_{31}, L_{32}, L_{33}, L_{34}, and L_{35}, where L_{31}, L_{32}, L_{33}, L_{34}, and L_{35} all have a width of W_3. The blue S-shaped structure consists of strips L_{41}, L_{42}, L_{43}, L_{44}, L_{45}, and L_{46}, each with a width of W_4.

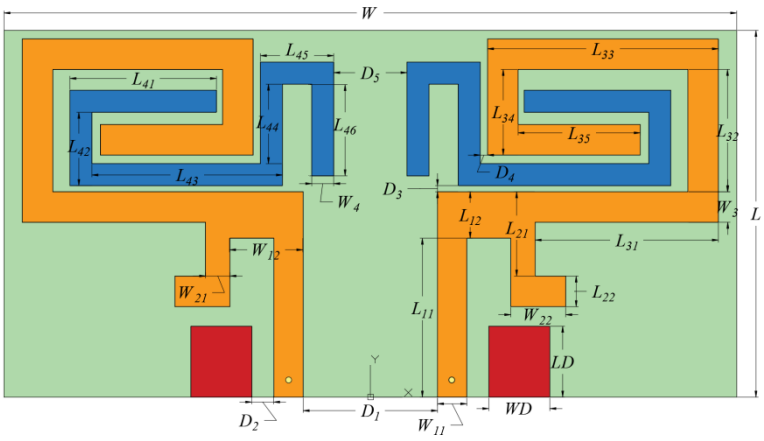


Figure 1. Schematic diagram of the antenna structure.

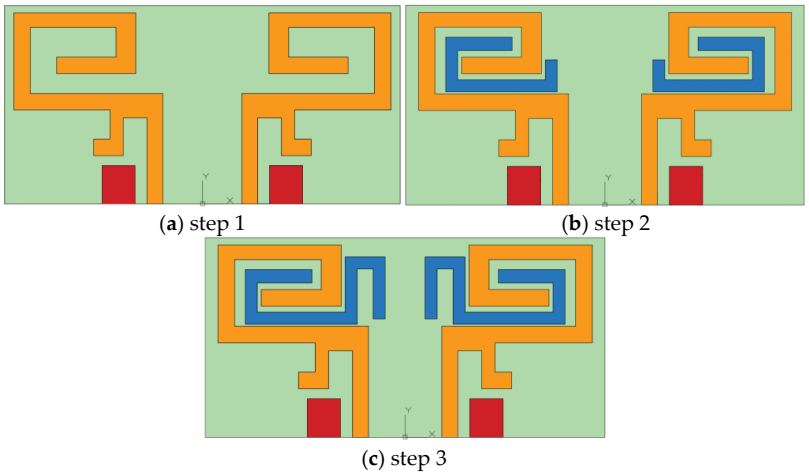
The loop structures are fed by separate quasi-coplanar waveguide structures, with only a single common ground structure retained, shown as the red portion in the figure. The feeding points, marked in yellow, are connected to the inner conductors of coaxial cables, while the ground points are soldered to the outer conductors. The S-shaped structures are excited by coupling from the corresponding loop structures, where segments L_{45} and L_{46} mainly serve a shielding function and L_{41}, L_{42}, L_{43}, and L_{44} are responsible for frequency tuning and control.

The overall dimensions of the antenna are 60 mm × 30 mm × 1.6 mm. The design target frequency bands of the proposed antenna are 2.40–2.73 GHz (ISM band) and 3.38–3.63 GHz (China 5G n78 Sub-6 GHz band), which are determined according to UAV communication requirements. The design is optimized using the Ansys HFSS (2020 R1) full-wave electromagnetic simulation software. The configuration and geometric parameters of the antenna are illustrated in Figure 1 and listed in Table 1, respectively.

Table 1. Geometric parameters of the proposed antenna.

Parameter	Value (mm)	Parameter	Value (mm)	Parameter	Value (mm)
W	60.0	L_{11}	13.0	L_{33}	18.9
L	30.0	W_{12}	6.0	L_{34}	7
D_1	11.0	L_{12}	3.8	L_{35}	10
D_2	1.8	W_{21}	2.0	W_4	1.8
D_3	0.5	L_{21}	6.9	L_{41}	12
D_4	0.6	W_{22}	4.5	L_{42}	6.4
D_5	6.0	L_{22}	2.5	L_{43}	15.6
WD	5.0	W_3	2.5	L_{44}	6.5
LD	5.8	L_{31}	15	L_{45}	6
W_{11}	2.4	L_{32}	10	L_{46}	7.5

The final antenna design proposed in this paper and its evolution process are shown in Figure 2, and the simulated S-parameter variations during the evolution are illustrated in Figure 3.



(**a**) step 1 (**b**) step 2

(**c**) step 3

Figure 2. Evolution process of the antenna.

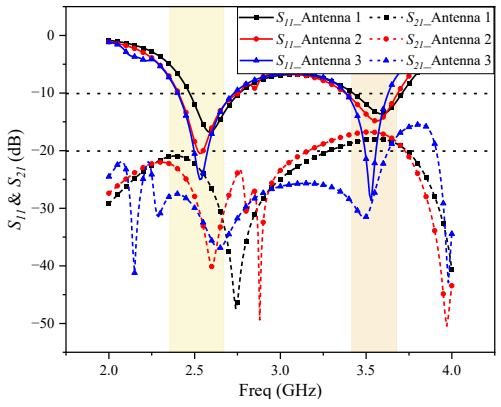


Figure 3. S-parameters during the entire evolution process.

In Step 1, a loop-strip antenna with stubs is designed and fed by a coplanar waveguide structure, in which only half of the ground plane is retained in the quasi-CPW feeding structure. The loop configuration reduces the physical size of the antenna and generates dual-band resonance within a limited space. The vector current distribution of Antenna 1 at 2.5 GHz is shown in Figure 4, where the current is mainly concentrated on the loop strip. The two current path lengths λ_{11} and λ_{12} can be obtained by Equations (1) and (2), respectively.

$$\lambda_{11} = [L_{11} + L_{12}] + [W_{12} + W_{21} + L_{31}] = 40.3\text{mm} \quad (1)$$

$$\lambda_{12} = L_{32} + [L_{33} - 2 \times W_3] + [L_{34} - 2 \times W_3] + L_{35} = 42.9\text{mm} \quad (2)$$

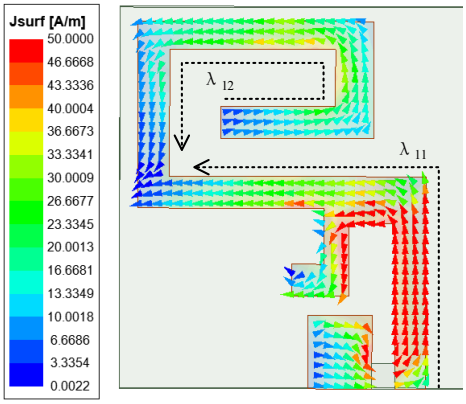


Figure 4. Vector current distribution of Antenna 1 at 2.5 GHz when the left element is excited.

The vector current distribution of Antenna 1 at 3.5 GHz is shown in Figure 5, where the current is mainly concentrated in the loop strip. The lengths of the two current paths λ_{21} and λ_{22} can be obtained by Equations (3) and (4), respectively.

$$\lambda_{21} = [W_{22} - W_{21}] + [L_{21} - W_3] + L_{31} + L_{32} = 31.9\text{mm} \quad (3)$$

$$\lambda_{22} = [L_{33} - W_3] + [L_{34} - 2 \times W_3] + L_{35} = 28.4\text{mm} \quad (4)$$

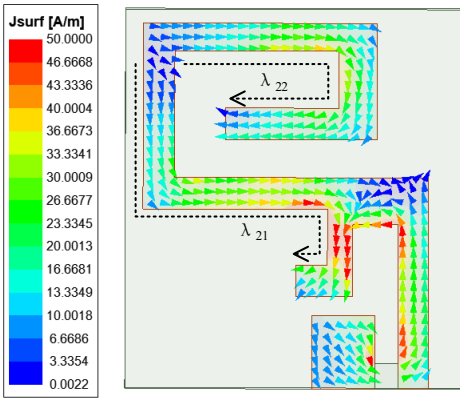


Figure 5. Vector current distribution of Antenna 1 at 3.5 GHz when the left element is fed.

The dielectric wavelength, λ_d, can be calculated using the following equation:

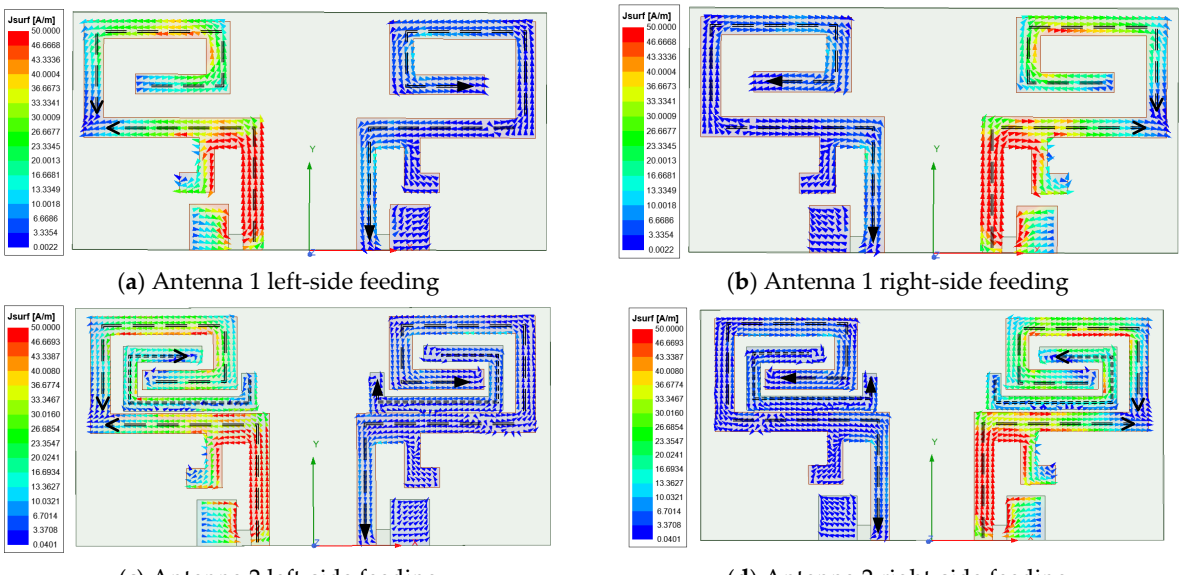
$$\lambda_d = \frac{c}{f\sqrt{\varepsilon_r}} \quad (5)$$

where c is the speed of light in a vacuum, f is the operating frequency, and ε_r is the relative permittivity of the dielectric substrate. The relative permittivity of the substrate used in this work is 4.4. Using Equation (5), the theoretical dielectric half-wavelengths at 2.5 GHz and 3.5 GHz are calculated to be 28.6 mm and 20.4 mm, respectively. Due to the coupling and bending effects between adjacent lines, the actual effective electrical length of the antenna is slightly smaller than the total physical length of the meandered strips. Therefore, λ_{11}, λ_{12}, λ_{21}, and λ_{22} are all larger than the theoretical dielectric half-wavelength. At both 2.5 GHz and 3.5 GHz, two current paths with approximately equal lengths but opposite directions exist on the antenna element, and the operating modes at these two bands resemble a pair of half-wavelength dipole antennas with identical wavelengths.

The resonant frequency can be tuned using stubs L_{21} and L_{22}. This antenna operates from 2.47 to 2.76 GHz and 3.42 to 3.71 GHz, covering the 5G band but failing to fully satisfy the requirements of the 2.4 GHz band. The structure achieves good isolation in the 2.4 GHz band, with S_{21} below -20 dB. However, S_{21} remains around -18 dB in the 5G band.

In Step 2, Antenna 2 is developed by adding a pair of C-shaped strips to Antenna 1. Antenna 2 covers the bands from 2.41 to 2.76 GHz and 3.38 to 3.69 GHz. The C-shaped strips are excited through electromagnetic coupling with the main loop radiator. Compared with Design 1, the lower frequency band around 2.4 GHz is shifted downward, fully covering the 2.4 GHz band. Meanwhile, the isolation within the 2.4 GHz band is significantly improved, with the minimum S_{21} reaching -40 dB. Nevertheless, the C-shaped strips exert little influence on the resonant characteristics and isolation of the 3.5 GHz band.

The downward frequency shift and enhanced isolation in the 2.4 GHz band introduced by the C-shaped strips can be clarified through electromagnetic field and current distribution analysis. Figure 6 shows the vector current distributions of Antenna 1 and Antenna 2 at 2.5 GHz with only one side element excited. At 2.5 GHz, both Antenna 1 and Antenna 2 can be regarded as half-wavelength dipole antennas, exhibiting the same current distribution on the main loop structure. After adding the C-shaped strips, increased current intensity is observed on L_{33} and W_{12}, indicating an extended effective current length, which results in the downward shift of the 2.4 GHz band and meets the application requirements.



(**a**) Antenna 1 left-side feeding (**b**) Antenna 1 right-side feeding

(**c**) Antenna 2 left-side feeding (**d**) Antenna 2 right-side feeding

Figure 6. Vector current distributions at 2.5 GHz with only a single antenna element excited.

The further improved isolation around 2.5 GHz can be explained as follows. As shown in Figure 6a, when only the left element of Antenna 1 is fed, the two vector current segments

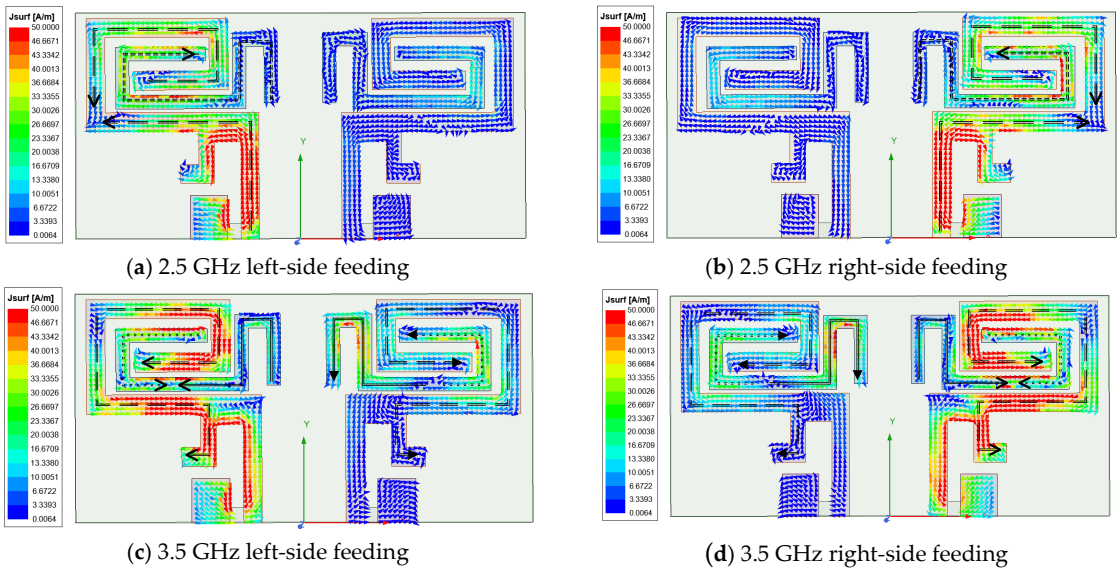
on the left loop stub rotate counterclockwise, and the coupled current on the right element also rotates counterclockwise. As shown in Figure 6b, when only the right element is fed, both the total vector current and the coupled current rotate clockwise. This indicates that the two antenna elements have opposite polarizations, enabling effective polarization diversity. The two antennas thus behave like loop antennas with different circular polarizations, effectively reducing the coupling between elements. The two antenna elements produce mutually orthogonal linear polarization. Due to the orthogonal polarization characteristics, the electromagnetic wave radiated from one port cannot be efficiently captured by the adjacent element, which suppresses spatial field coupling and improves port isolation, realizing linear polarization diversity.

During simultaneous operation, the opposite current rotation directions on the two elements allow mutual interference-free operation. However, certain mutual coupling still exists under single-port excitation, which limits the isolation improvement. After adding the C-shaped structure, the current direction with only the left port excited is shown in Figure 6c: the current on the left loop and the coupled current on the right loop are both counterclockwise, while a strong clockwise current is induced on the adjacent C-shaped strips. Similarly, as shown in Figure 6d, with only the right port excited, the currents on both loops are clockwise, while a strong counterclockwise current is induced on the C-shaped strips. The length of the C-shaped strip is approximately equal to λ_{12}, and its current direction is opposite to that of the loop structure. Therefore, the introduction of the C-shaped strips greatly reduces the energy coupled outward from the loop strips, achieving further improved isolation.

In Step 3, Antenna 3 is developed by replacing the C-shaped strips with S-shaped strips based on Antenna 2, which significantly improves both the impedance matching and isolation performance at 3.5 GHz. It should be clarified that the S-shaped strips are not additional decoupling structures independently introduced after the radiator design is finalized but an inherent component of the overall radiating topology. They are excited by the coupling of the main loop radiator and jointly participate in the construction of the antenna's dual-band operating modes while realizing the self-decoupling function. The final antenna operates in the bands of 2.40–2.73 GHz and 3.38–3.63 GHz. This structure ensures good isolation in the 2.4 GHz band, with S_{21} below -27 dB, and in the 5G band, S_{21} is below -20 dB. The distance, D_5, between the two S-shaped structures is 6 mm, approximately 1/14 of the wavelength at 3.5 GHz. It meets the application requirements of both the 2.4 GHz band and the 5G band and maintains excellent isolation in both bands.

The mechanism by which the S-shaped strips enhance isolation in the 3.5 GHz band is illustrated in Figure 7. Compared with the current intensity under single-port excitation at 2.5 GHz, the coupled current on the S-shaped strips at 3.5 GHz increases. A segment of current with a rotation direction different from that on the loop strips is generated on L_{41}, L_{42}, and part of L_{43}, which weakens the energy coupled outward from the loop strips. Meanwhile, a segment of current with the opposite direction and a lower intensity is induced on parts of L_{43}, L_{44}, and L_{45}. This segment counteracts the unblocked energy and is opposite to the remaining coupled current. Additionally, the meandering structure of this segment extends the transmission path of the coupled energy, enhancing the natural attenuation of electromagnetic energy during propagation and further reducing the intensity of the leaked energy.

This design enables Antenna 3 to achieve a port isolation greater than 20 dB in the 5G band (3.38–3.63 GHz) while maintaining a high isolation level above 27 dB in the 2.4 GHz Wi-Fi band. Ultimately, good impedance matching and port isolation are achieved in a compact layout, providing a simple and efficient solution for the design of multi-band MIMO antennas.



(**a**) 2.5 GHz left-side feeding (**b**) 2.5 GHz right-side feeding

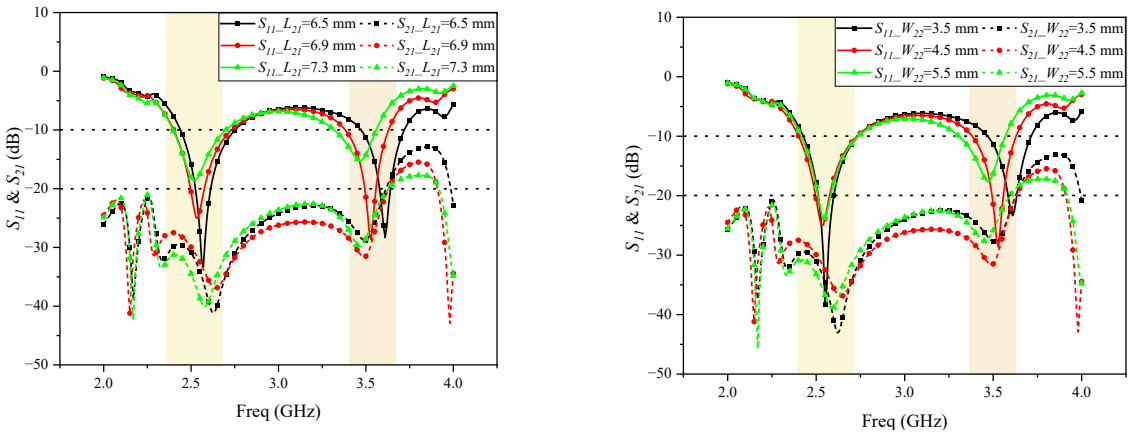
(**c**) 3.5 GHz left-side feeding (**d**) 3.5 GHz right-side feeding

Figure 7. Vector current distribution of Antenna 3 with only a single element excited.

3. Parametric Analysis

To obtain ideal operating bands and good isolation, parametric analysis is conducted on the length of the loop strip, the length of the S-shaped strip, and the gap between them in this section.

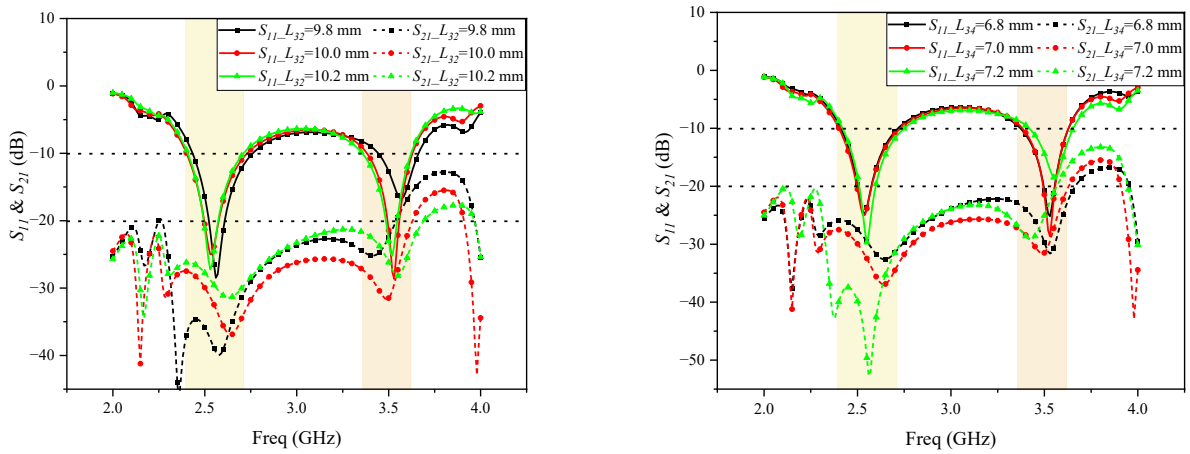
Figure 8 shows the effect of stub length on the antenna S-parameters. The antenna operates in dipole mode at 3.5 GHz, and its two arms are composed of (L_{33} + L_{34} + L_{35}) and (L_{31} + L_{32} + L_{21} + W_{22}), respectively. Therefore, the dimensional changes of L_{21} and W_{22} significantly regulate the S_{11} of the 3.5 GHz band and also exert a certain influence on S_{21}, though not as a dominant factor. Figure 8a shows the effect of L_{21} on the antenna S-parameters. Increasing L_{21} from 6.5 mm to 7.3 mm significantly increases the S_{11} value in the 2.4 GHz band, deteriorating the impedance matching. However, this length variation has little effect on the position of the 2.4 GHz resonance point. In the 3.5 GHz band, the resonant frequency shifts to lower frequencies as L_{21} increases, and the impedance matching performance first improves and then deteriorates. As shown in Figure 8b, during the increase in W_{22} from 3.5 mm to 5.5 mm, its effect on the S_{11} parameter is similar to that of L_{21}, both showing a significant regulatory effect on the resonant frequency and impedance matching state. Therefore, L_{21} = 6.9 mm and W_{22} = 4.5 mm are selected as the final optimized values to ensure good impedance matching in both bands.



(**a**) Effect of L21 dimension on the S-parameters of the antenna(**b**) Effect of W22 dimension on the S-parameters of the antenna

Figure 8. Effects of stub lengths on the antenna S-parameters.

Figure 9 investigates the effects of the vertical loop stub lengths L_{32} and L_{34} on the S-parameters.



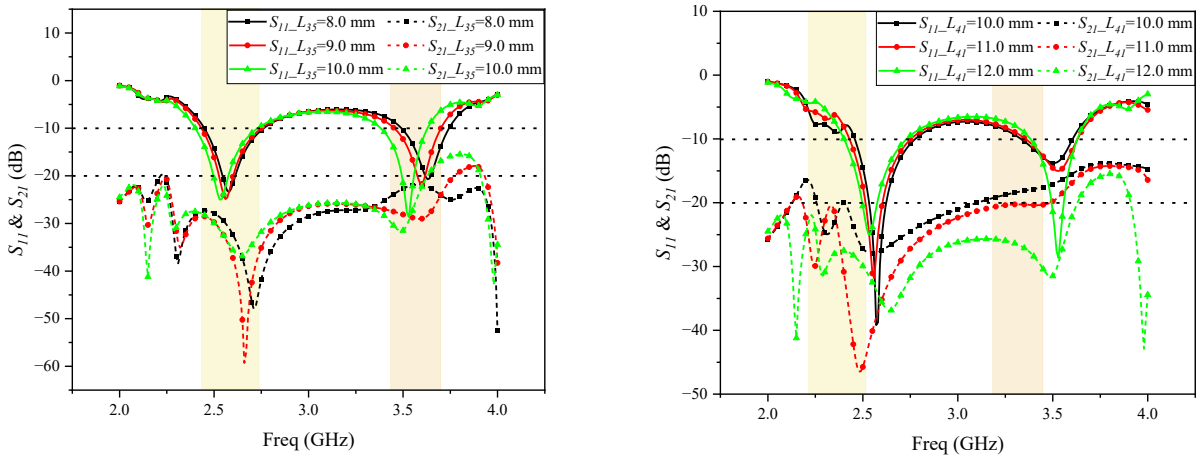
(**a**) Effect of L_{32} dimension on the S-parameters of the antenna(**b**) Effect of L_{34} dimension on the S-parameters of the antenna

Figure 9. Effects of vertical loop stub lengths on the S-parameters.

These two key dimensions directly determine the spatial distance between the main loop stub and the adjacent S-shaped coupling stub, thereby regulating the strength of electromagnetic coupling between them. The amplitude variation of the coupling current further affects the energy leakage between antenna ports, so L_{32} and L_{34} play a key tuning role in the isolation S_{21}. In Figure 9a, as L_{32} increases from 9.8 mm to 10.2 mm, the distance between L_{31} and L_{41} increases, weakening the coupling current intensity, while the distance between L_{35} and L_{41} decreases, enhancing the coupling current intensity. The 2.4 GHz band slightly shifts to lower frequencies, and its S_{21} increases with the increase in L_{32}, resulting in decreased isolation. The 3.5 GHz band also slightly shifts to lower frequencies, and the impedance matching is improved. Its S_{21} first decreases and then increases with the increase in L_{32}, and the isolation first increases and then decreases. In Figure 9b, as L_{34} increases from 6.8 mm to 7.2 mm, the distance between L_{35} and L_{41} increases, weakening the coupling current intensity, while the distance to L_{43} decreases, enhancing the coupling current intensity. The 2.4 GHz band slightly shifts to higher frequencies, and its S_{21} decreases with the increase in L_{32}, resulting in increased isolation. The 3.5 GHz band slightly shifts to higher frequencies, and its S_{21} first decreases and then increases with the increase in L_{34}, and the isolation is first optimized and then deteriorated. Based on the above analysis, the variations in L_{32} and L_{34} have complex and interrelated effects on the impedance matching and isolation of the dual bands. Therefore, L_{32} = 10.0 mm and L_{34} = 7.0 mm are selected as the final optimized values to achieve acceptable matching performance and a good isolation effect in both operating bands while effectively controlling the coupling strength.

Figure 10 shows the effects of the coupling length between the loop strip and the S-shaped strip on the S-parameters. These two parameters directly regulate the interaction strength and current distribution between the radiator and the coupling structure. Figure 10a shows the effect of L_{35} on the antenna S-parameters. As L_{35} increases from 8.0 mm to 10.0 mm, the coupling length with L_{41} and L_{43} increases, and the resonant frequency in the 2.4 GHz band slightly shifts to lower frequencies, with S_{21} first decreasing and then increasing. In the 3.5 GHz band, the resonant frequency significantly shifts to lower frequencies as L_{35} increases, and the impedance matching at this frequency is significantly improved. S_{21} decreases with the increase in L_{35} in this band, resulting in increased isolation. As shown in Figure 10b, during the increase in L_{41} from 10.0 mm to

12.0 mm, the coupling length with L_{33} and L_{35} increases, the 2.4 GHz band slightly shifts to lower frequencies, and the impedance matching deteriorates. The isolation variation in this band is similar to that affected by L_{33}. The variation in the L_{41} length has little effect on the resonant frequency position but greatly improves the impedance matching. S_{21} decreases with the increase in L_{41}. Therefore, L_{35} = 10.0 mm and L_{41} = 12.0 mm are comprehensively selected as the final optimized values, achieving good port isolation while ensuring excellent impedance matching in both operating bands.



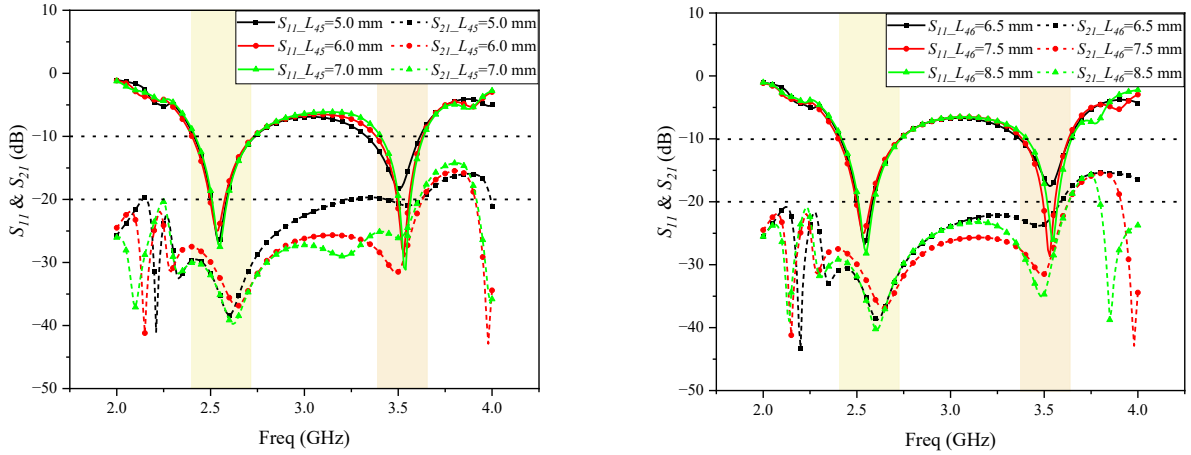
(**a**)Effect of L35 dimension on the S-parameters of the antenna(**b**) Effect of L41 dimension on the S-parameters of the antenna

Figure 10. Effects of coupling length between the loop strip and the S-shaped strip on the S-parameters.

Figure 11 shows the effects of S-shaped strip lengths on the antenna S-parameters. The two parameters L_{45} and L_{46} mainly function to adjust the port isolation of the antenna in the 3.5 GHz operating band, while their effects on the impedance matching and isolation of the 2.4 GHz band are not significant. As depicted in Figure 11a, when the length of L45 increases from 5.0 mm to 7.0 mm, the physical spacing between two radiating elements is reduced. The narrowed gap intensifies near-field electromagnetic coupling between antenna units, which is unfavorable for isolation improvement. In addition, the prolonged coupling current path optimizes the impedance matching at 3.5 GHz. Consequently, the S21 parameter first declines and then rises as L45 increases, leading to a trend that the port isolation is enhanced initially and degraded afterwards. Figure 11b presents the performance variation with the length of L46 ranging from 6.5 mm to 8.5 mm. Distinct from L45, L46 serves as an effective shielding component to block the coupled electromagnetic energy between elements, and it dominates the isolation characteristic of the proposed MIMO antenna. As L46 increases, the S11 curve presents a trend of first decreasing and then increasing, whereas S21 keeps decreasing continuously. This indicates that a longer L46 can effectively suppress mutual coupling and further improve port isolation. This combination ensures stable performance in the 2.4 GHz band while achieving good impedance matching and excellent isolation in the 3.5 GHz band, meeting the requirements of the antenna system for dual-band high-performance operation.

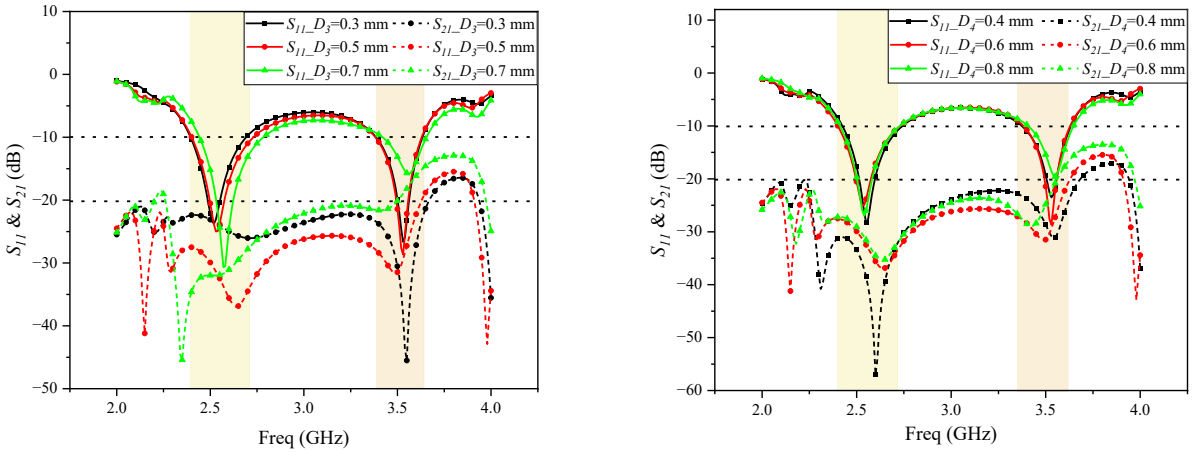
Figure 12 shows the parametric analysis of the gaps between the loop strip and the S-shaped strip. These two gap parameters determine the spatial distance between the coupling structures, thereby significantly affecting the strength of their electromagnetic coupling and exerting an obvious influence on the resonant characteristics and port isolation of the antenna. Figure 12a shows the effect of the distance, D_3, between strips L_{31} and L_{43} on the antenna S-parameters. As D_3 increases, the distance between coupling strips L_{43} and L_{31} increases, weakening the coupling current intensity, while the distance to L_{35} decreases, enhancing the coupling current intensity. In the 2.4 GHz band, the resonant frequency

shifts to higher frequencies as D_3 increases, and the impedance matching is improved. Its S_{21} decreases with the increase in D_3, improving the isolation performance. The 3.5 GHz band also slightly shifts to higher frequencies, the impedance matching deteriorates, and its S_{21} increases with the increase in D_3, weakening the isolation. Figure 12b shows the effect of the distance, D_4, between strips L_{34} and L_{44} on the antenna S-parameters. As D_4 increases from 0.4 mm to 0.8 mm, the distance between L_{44} and L_{34} increases, weakening the coupling current. S_{11} in the 2.4 GHz band remains basically unchanged; its S_{21} increases with the increase in D_4, deteriorating the isolation. The impedance matching at 3.5 GHz first increases and then decreases, and its S_{21} increases with the increase in D_4, deteriorating the isolation. Based on the above analysis, the variations in D_3 and D_4 affect the impedance matching and isolation of both bands. Therefore, D_3 = 0.5 mm and D_4 = 0.6 mm are selected as the final gap values. This combination effectively balances the coupling strength between the two bands with acceptable impedance matching, achieving better overall isolation performance.



(**a**) Effect of L45 dimension on the S-parameters of the antenna(**b**) Effect of L46 dimension on the S-parameters of the antenna

Figure 11. Effects of S-shaped strip lengths on the S-parameters.



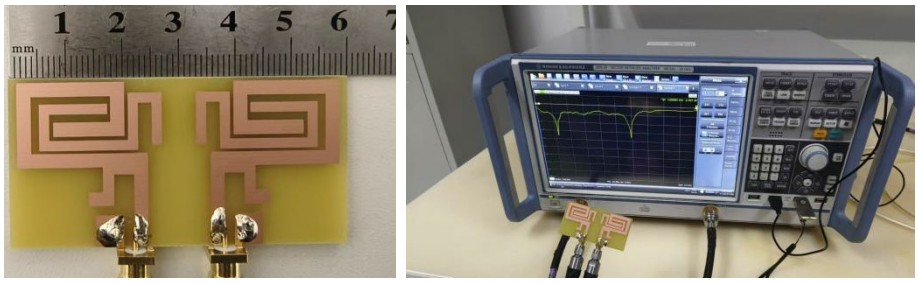
(**a**) Effect of D3 dimension on the S-parameters of the antenna(**b**) Effect of D4 dimension on the S-parameters of the antenna

Figure 12. Effects of gaps between the loop strip and the S-shaped strip on the S-parameters.

4. Comparison and Analysis of Simulated and Measured Antenna Results

Figure 13a shows the physical antenna dimensions, and its performance was tested using a Rohde & Schwarz ZNB20 vector network analyzer. The test environment is shown

in Figure 13b. Figure 14 shows the comparison between simulated and measured S-parameters of the antenna. It can be observed that within the two target frequency bands, the simulated and measured S_{11} results are in good agreement in the overall trend. Both bands shift to higher frequencies by approximately 40 MHz, with frequency ranges of 2.44–2.69 GHz and 3.36–3.68 GHz. The measured upper band still fully covers the core bandwidth of China's 5G NR n78 band and satisfies regional 5G UAV communication requirements. The measured minimum S_{11} at the center frequency of the lower band reaches −58.5 dB, and that at the center frequency of the higher band reaches −34.2 dB. The simulated and measured S_{21} results shift to the left by approximately 0.2 GHz in the lower band and are significantly improved in the higher band. The S_{21} values at the two frequency points are −33.3 dB and −27.7 dB, respectively, and the isolation is greater than 20 dB across the entire application band, meeting engineering requirements. The original simulated bandwidth of the bare antenna is 2.33–2.63 GHz (lower band) and 3.21–3.47 GHz (upper band). After fabrication, the measured bandwidth of the physical prototype is 2.44–2.69 GHz and 3.36–3.68 GHz. The discrepancy between simulation and measurement is mainly caused by PCB etching tolerance, parasitic capacitance introduced by coaxial soldering and assembly errors. Specifically, the measured lower band is about 20% wider than the simulated one, while the measured upper band is reduced by approximately 19%. Such bandwidth discrepancy mainly stems from PCB fabrication tolerance of metal strip width and clearance deviation, as well as parasitic capacitance introduced by coaxial soldering during prototype assembly. PCB etching tolerances of the S-shaped coupling strips and radiating arms may cause local line width and gap dimensions to deviate from the design values, changing the equivalent inductance and capacitance of the antenna and thus affecting the resonant frequency. In addition, slight misalignment during the assembly of the coaxial connector may generate parasitic capacitance, changing the impedance matching condition at the feeding point and further affecting the resonant characteristics of the antenna.



(**a**) Physical photograph of the antenna (**b**) Diagram of the antenna test environment

Figure 13. Antenna prototype and test environment.

Figures 15 and 16 show the comparison between simulated and measured radiation patterns of the antenna in the xoy-plane and the xoz-plane at 2.5 GHz and 3.5 GHz, respectively. In the xoy-plane at both bands, the radiation patterns are approximately figure-eight-shaped and exhibit good polarization purity, with cross-polarization less than −30 dB at 2.5 GHz and less than −25 dB at 3.5 GHz. The radiation pattern at 3.5 GHz shows a certain distortion in the 240° direction. In the xoz-plane, the radiation patterns of both bands are slightly different but generally maintain good omnidirectional radiation characteristics. Although the measured results are generally consistent with the simulated trends, slight distortions and amplitude deviations in the radiation patterns are still observed. These minor differences can be attributed to vector network analyzer calibration and probe position errors during the measurement, which slightly affect the

symmetry and gain level of the patterns. The basic radiation characteristics of the antenna are still well maintained, verifying its ability to maintain a stable signal connection.

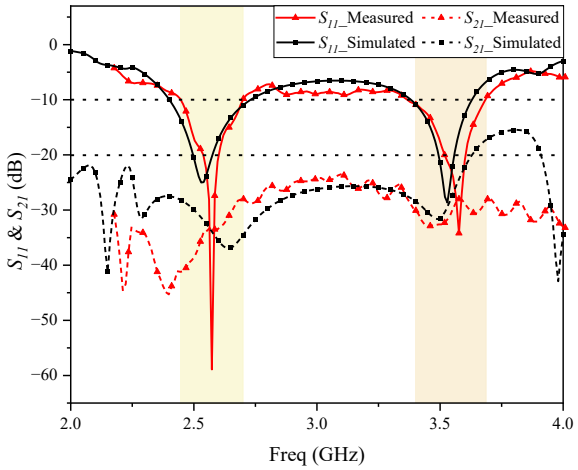
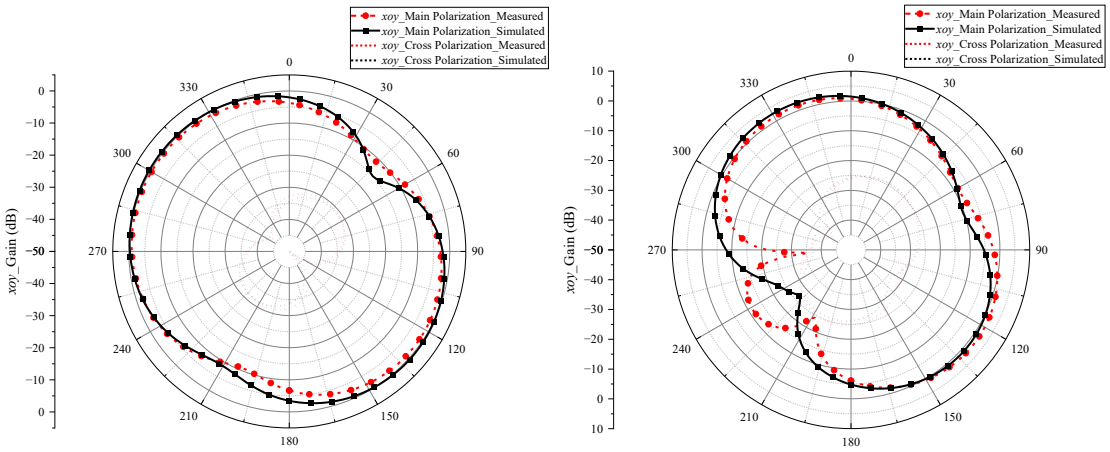
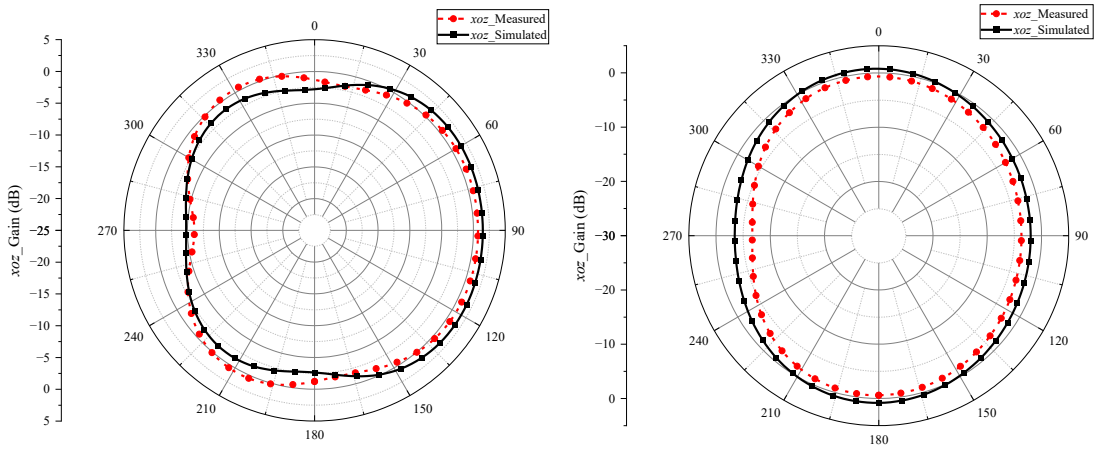


Figure 14. Comparison of simulated and measured S-parameters of the antenna.



(**a**) 2.5 GHz (**b**) 3.5 GHz

Figure 15. Radiation patterns in the xoy-plane.



(**a**) 2.5 GHz (**b**) 3.5 GHz

Figure 16. Radiation patterns in the xoz-plane.

Figure 17 shows the gain and radiation efficiency curves of the antenna. The antenna gain is approximately 0.7–1.5 dB in the 2.4 GHz operating band and approximately 2.3–2.9 dB in the 3.5 GHz operating band. The radiation efficiency data provided in this paper were obtained through HFSS simulation. The radiation efficiency is higher than 90% in the 2.4 GHz operating band and greater than 80% in the 3.5 GHz operating band. The antenna maintains good radiation characteristics and favorable gain within the operating bands.

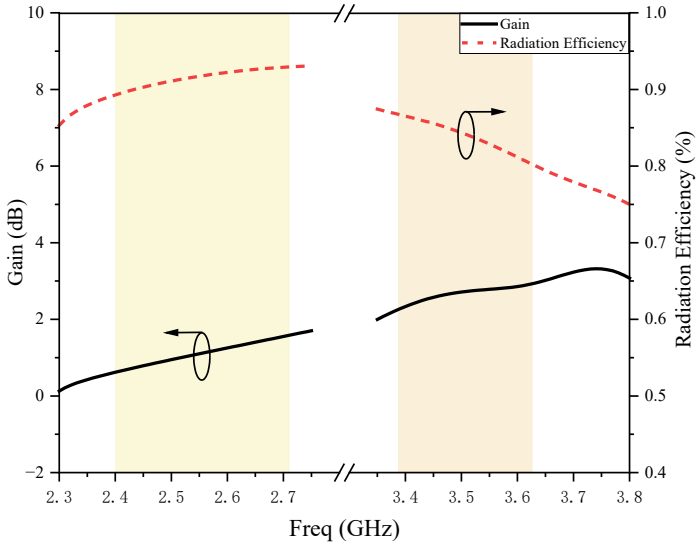


Figure 17. Antenna gain and radiation efficiency.

Constrained by the compact overall dimensions, the antenna has an inherently limited theoretical upper gain. The measured gain ranges from 0.7 to 1.5 dB at 2.4 GHz and 2.3 to 2.9 dB at 3.5 GHz. Additional extrinsic losses, including insertion loss of coaxial connectors, feedline attenuation and multipath stray losses from the test environment, further degrade the measured gain. The simulated radiation efficiency exceeds 90% in the lower band and 80% in the upper band, which verifies the favorable inherent radiation performance of the antenna. The relatively low measured gain is mainly attributed to various test-related losses rather than poor intrinsic radiation capability.

The envelope correlation coefficient (ECC) of the antenna is shown in Figure 18. The data were obtained using the ECC formula (6) based on three-dimensional patterns:

$$ECC = \frac{\left| \iint_{4\pi} \left[\vec{F}_1^*(\theta,\phi) \cdot \vec{F}_2^*(\theta,\phi) \right] d\Omega \right|^2}{\iint_{4\pi} \left| \vec{F}_1(\theta,\phi) \right|^2 d\Omega \cdot \iint_{4\pi} \left| \vec{F}_2(\theta,\phi) \right|^2 d\Omega} \quad (6)$$

where * denotes the Hermitian product; $\vec{F}_1(\theta,\phi)$ and $\vec{F}_2(\theta,\phi)$ are the three-dimensional radiation patterns of the antenna when the first and second ports are excited, respectively; and is the solid angle of the antenna. The ECC of the antenna system reaches a low level in both bands, less than 0.15, indicating that the designed antenna has good signal independence. This enables the antenna system to effectively support dual-mode operation of Wi-Fi and 5G, meeting the requirements of modern wireless communication systems for multi-band, high-capacity transmission.

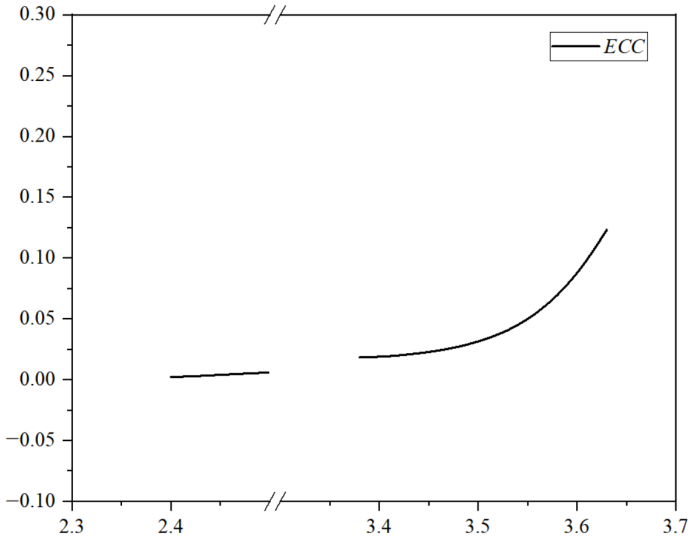


Figure 18. Antenna ECC.

To further quantitatively evaluate the diversity performance of the MIMO antenna in multipath fading environments, diversity gain (DG) is introduced as another essential MIMO performance metric. The DG characterizes the maximum received power gain that the diversity system can provide compared with a single-antenna system under isotropic random incident waves.

Diversity gain (DG) is calculated using the following formula:

$$\mathrm{DG} = 10\sqrt{1 - ECC^2} \tag{7}$$

Calculation results demonstrate that the DG maintains a high level in both target operating bands, remaining above 9.9 dB over the entire 2.40–2.73 GHz ISM band and 3.38–3.63 GHz 5G n78 band, which approaches the theoretical ideal value of 10 dB for a dual-channel diversity system. Benefiting from the orthogonal linear polarization design and low mutual coupling between elements, the high diversity gain can effectively combat signal fading caused by multipath propagation and UAV attitude fluctuations in practical communication scenarios.

Table 2 presents the performance comparison between the proposed UAV multi-band MIMO antenna design and related antennas in the existing literature. It can be seen from the table that compared with other designs in the literature, the proposed design achieves a more compact layout in terms of electrical size, with an overall size of $0.48 \times 0.24 \times 0.013\ \lambda_L$, smaller than most similar schemes. At the same time, it uses relatively low-cost FR-4 as the substrate material, effectively controlling the manufacturing cost. Compared with the reference literature, the proposed design has a smaller number of antenna elements (two elements), making the isolation index easier to achieve. However, without introducing additional decoupling structures, the proposed design achieves omnidirectional radiation characteristics in both target bands of 2.40–2.73 GHz and 3.38–3.63 GHz, with port isolation better than 27 dB and 20 dB, respectively, which can effectively support the stable communication requirements of small UAVs in multi-band scenarios, achieving a good balance between size, cost, and performance.

Table 2. Performance comparison between the proposed design and other UAV multi-band MIMO antennas.

Comparison	Electrical Size (λ_L)	Frequency Band (GHz)	Isolation (dB)	Gain (dB)
[11]	0.93 × 0.93 × 0.005	2.04~3.25 5.37~7.38	>23 >19	2.97 5.94
[12]	0.49 × 0.49 × 0.0009	2.07~2.84 4.89~6.99	>13 >25	2.6
		8.19~9.10 10.22~11.19	>30 >30	5.2
[13]	1.16 × 1.16 × 0.0128	2.47~2.51 5.09~5.26	>25 >33	9.55 8.50
[14]	0.39 × 3.99 × 0.002	2.0~2.5 4.4~4.7	-	0.8 0
This paper	0.48 × 0.24 × 0.013	2.40~2.73 3.38~3.63	>20 >20	1.2 2.5
Comparison	High-isolation techniques	Substrate material	Number of layers	Number of elements
[11]	Orthogonal arrangement	Rogers RT5880	Single layer	4
[12]	Orthogonal arrangement; centrally slotted ring and back dumbbell-shaped structure	Polyimide	Single layer	4
[13]	Increase inter-element spacing	Roger 5880	Double layer	3
[14]	Increase inter-element spacing	Rogers 3003	Double layer	4
This paper	Self-isolation	FR-4	Single layer	2

5. Practical Antenna Applications

5.1. Antenna Encapsulation

In practical applications, the antenna needs to be encapsulated to avoid corrosion and other problems. Figure 19 shows the schematic diagram of the antenna encapsulated with low-dielectric-constant epoxy adhesive (Jinshida K-3646, relative permittivity: 2.35). Except for the feeding area of the connector and its lower surface, the rest of the antenna is completely encapsulated. The thickness of the encapsulated part is 0.2 mm. Figure 20 shows the effect of encapsulation on the antenna S-parameters. Both bands of the antenna shift to lower frequencies after encapsulation, but the resonant characteristics remain unchanged. The left shift of the 3.5 GHz band is more obvious than that of the 2.5 GHz band. The impedance matching of both bands is slightly worse than that before encapsulation, with bandwidths of 2.38–2.70 GHz and 3.33–3.54 GHz, which still fully cover the ISM band and China's 5G NR n78 band for civil UAV communication services. After encapsulation, the S_{21} parameter remains below −15 dB within the band (simulated data), slightly higher than before encapsulation, but still maintains good isolation.

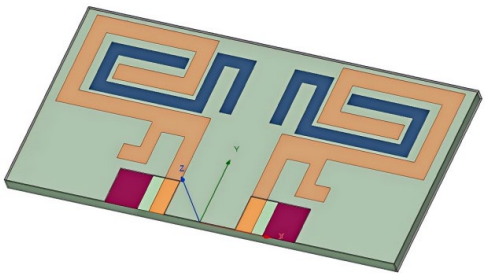


Figure 19. Schematic diagram of antenna encapsulation.

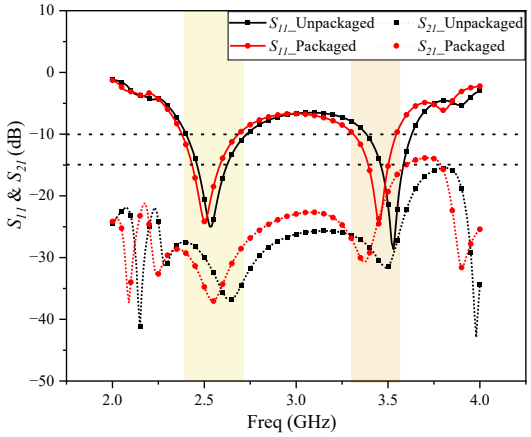


Figure 20. S-parameter plots of the antenna before and after packaging.

5.2. Co-Simulation with UAV

The encapsulated antenna is installed on an eight-rotor tethered UAV for emergency communications. The UAV fuselage size is much larger than the antenna and the operating frequency. The UAV is modeled assuming that the fuselage is made of plastic material (relative permittivity: 2.7, loss tangent: 0.007). The antenna is installed on the top of the fuselage to avoid electromagnetic interference from internal structures such as the motherboard and battery, with a fuselage thickness of 1.5 mm. The area of the UAV where the antenna is installed has a local wall thickness of 0.5 mm to ensure efficient signal transmission. The simulation diagram of the antenna installed on the top of the UAV is shown in Figure 21.

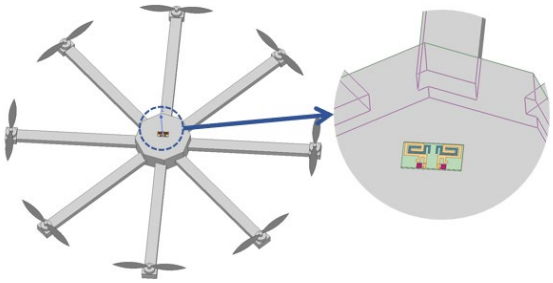


Figure 21. Simulation diagram of antenna installed on the top of the UAV.

This part is completed by electromagnetic co-simulation instead of a real UAV installation and flight test. For practical UAV deployment, concrete installation guidelines are supplemented in this work. The antenna is mounted on the top of the drone's plastic fuselage and kept far away from internal flight control circuits and batteries to mitigate unwanted electromagnetic interference. The original 1.5 mm thick fuselage shell is locally reduced to 0.5 mm underneath the antenna position to cut down dielectric loss and frequency drift. Prior to installation, the antenna is fully encapsulated by 0.2 mm low-permittivity epoxy resin, except for feed connectors, which protects the metal patch against dampness, abrasion and oxidation during outdoor flight. After encapsulation and fuselage integration, the antenna still features over 15 dB port isolation across the target bands and stable omnidirectional radiation, well satisfying the practical demands of UAV flight control and 5G data communication.

Figure 22 shows the effect of the encapsulated antenna installed on the UAV support on its S-parameters compared with the unencapsulated state. After being installed on the UAV, the overall operating band further shifts to lower frequencies. The impedance matching in the 2.5 GHz band decreases, with the S_{11} value 5 dB higher than that of the only

encapsulated antenna, and the S_{11} at the resonance point reaches −20 dB. The impedance matching in the 3.5 GHz band is improved compared with the only encapsulated antenna, with the S_{11} at the resonance point reaching −30 dB. When the encapsulated antenna is integrated with the virtual eight-rotor UAV (electromagnetic co-simulation), the final operating bandwidth is 2.30–2.59 GHz (lower band) and 3.25–3.52 GHz (upper band). The overall frequency performance still meets the design targets for UAV communication. The S_{21} parameter is below −20 dB in the 2.5 GHz band. In the 3.5 GHz band, S_{21} increases with encapsulation and installation on the fuselage, and the isolation decreases but remains higher than 15 dB within the band, meeting the application requirements of UAVs.

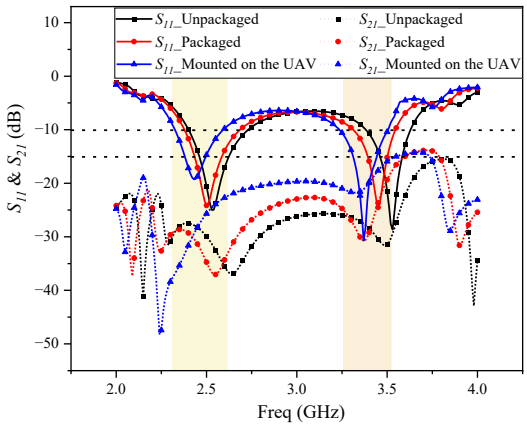
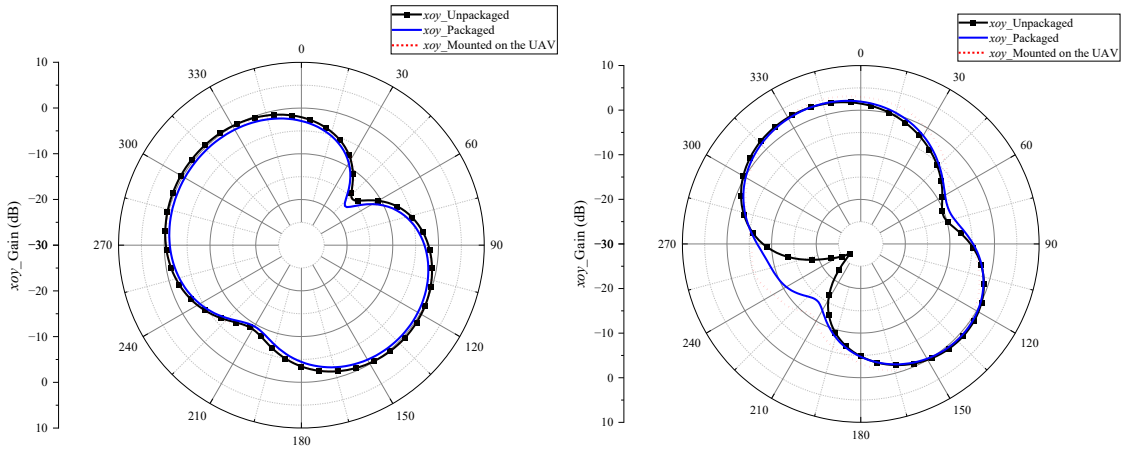


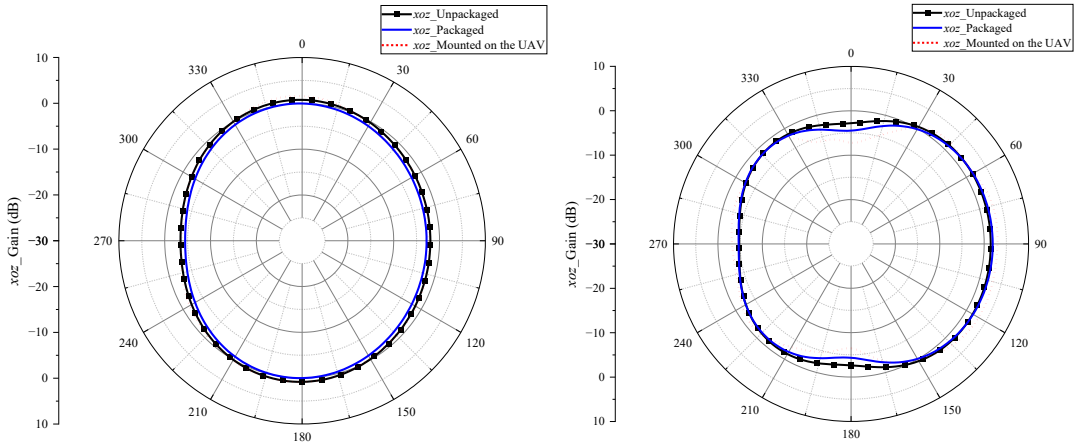
Figure 22. Effects of encapsulation and installation on the top of the UAV on the antenna S-parameters.

Figures 23 and 24 show the effects of encapsulation and installation on the UAV support on the radiation patterns of the antenna in the xoy-plane and the xoz-plane at 2.5 GHz and 3.5 GHz, respectively. At 2.5 GHz, the radiation patterns of the antenna installed on the UAV before and after encapsulation are basically the same, and the gain remains basically stable. At 3.5 GHz, the radiation patterns in the xoz-plane after encapsulation are basically the same as those before encapsulation, while the radiation patterns of the antenna installed on the UAV support show slight distortion but generally maintain good omnidirectionality within the operating band. In the xoy-plane, with encapsulation and installation on the UAV, the gain increases in the 240° direction, still generally meeting the requirements of UAV applications.



(**a**) 2.5 GHz (**b**) 3.5 GHz

Figure 23. Effects of encapsulation and installation on UAV support on the radiation patterns in the xoy-plane.



(**a**) 2.5 GHz (**b**) 3.5 GHz

Figure 24. Effects of encapsulation and installation on UAV support on the radiation patterns in the xoz-plane.

6. Conclusions

A two-element dual-band CPW-fed MIMO antenna is proposed for UAV applications, which achieves passive self-decoupling through the coupled loop strips and S-shaped strips. The S-shaped strips serve as an inherent part of the radiator rather than dedicated additional decoupling structures and play a role in both dual-band resonance tuning and mutual coupling suppression. The antenna has compact dimensions of 60 × 30 × 1.6 mm. The antenna is designed for the target bands of 2.40–2.73 GHz (ISM) and 3.38–3.63 GHz (5G n78). For the bare prototype, the simulated bandwidth is 2.33–2.63 GHz and 3.21–3.47 GHz, and the measured bandwidth is 2.44–2.69 GHz and 3.36–3.68 GHz. After epoxy encapsulation, the simulated bandwidth becomes 2.38–2.70 GHz and 3.33–3.54 GHz. When mounted on a virtual UAV model via co-simulation, the bandwidth is 2.30–2.59 GHz and 3.25–3.52 GHz. All results can satisfy UAV dual-band communication requirements. The isolation exceeds 27 dB within the 2.4 GHz band and 20 dB for the 3.5 GHz band, while the envelope correlation coefficient (ECC) remains below 0.15 and the diversity gain (DG) is higher than 9.9 dB throughout the operating frequencies. The measured realized gain is 0.7–1.5 dB in the lower band and 2.3–2.9 dB in the upper band. The radiation efficiency calculated by ANSYS HFSS simulation is higher than 90% and 80% for the two operating bands respectively. The fabricated prototype maintains favorable electrical specifications after being integrated into the UAV fuselage, enabling dual-mode communication for 5G Sub-6 GHz and 2.4 GHz ISM services. The fabricated prototype maintains favorable electrical specifications in standalone tests. Its performance after UAV fuselage integration is verified by co-simulation. This scheme provides a miniaturized dual-band MIMO antenna reference for UAV-assisted communication research.

Author Contributions: Y.H.: methodology, software, validation, formal analysis, investigation, writing—original draft preparation, writing—review and editing. Y.L.: software, validation. J.D.: software, validation. P.R.: software, validation. Y.F.: software, validation. L.Y.: writing—review and editing, resources, supervision, project administration, funding acquisition. All authors have read and agreed to the published version of the manuscript.

Funding: This research received no external funding.

Institutional Review Board Statement: Not applicable.

Informed Consent Statement: Not applicable.

Data Availability Statement: The data presented in this study are available on request from the corresponding author.

Conflicts of Interest: The authors declare no conflicts of interest.

References

1. Wu, H.; Wen, Y.; Zhang, J.; Wei, Z.; Zhang, N.; Tao, X. Energy-efficient and secure air-to-ground communication with jittering UAV. *IEEE Trans. Veh. Technol.* **2020**, *69*, 3954–3967. [CrossRef]
2. Hosseini, N.; Jamal, H.; Haque, J.; Magesacher, T.; Matolak, D.W. UAV command and control, navigation and surveillance: A review of potential 5G and satellite systems. In *Proceedings of the 2019 IEEE Aerospace Conference, Big Sky, MT, USA, 2–9 March 2019*; IEEE: New York, NY, USA, 2019; pp. 1–10.
3. Wu, Q.; Xu, J.; Zeng, Y.; Ng, D.W.K.; Al-Dhahir, N.; Schober, R.; Swindlehurst, A.L. A comprehensive overview on 5G-and-beyond networks with UAVs: From communications to sensing and intelligence. *IEEE J. Sel. Areas Commun.* **2021**, *39*, 2912–2945.
4. Altakhaineh, A.; Alsarayreh, S.; Alrawashdeh, R.; Rabie, K.; Sharari, F. A survey of limitations and future directions of antenna design for UAV applications. In *Proceedings of the 2024 14th International Symposium on Communication Systems, Networks and Digital Signal Processing (CSNDSP), Rome, Italy, 17–19 July 2024*; IEEE: New York, NY, USA, 2024; pp. 306–311.
5. Wang, S.; Kong, F.; Li, K.; Du, L. A planar triple-band monopole antenna loaded with an arc-shaped defected ground plane for WLAN/WiMAX applications. *Int. J. Microw. Wirel. Technol.* **2021**, *13*, 381–389.
6. Arpaio, M.J.; Paolini, G.; Fuschini, F.; Costanzo, A.; Masotti, D. An all-in-one dual band blade antenna for ADS-B and 5G communications in UAV assisted wireless networks. *Sensors* **2021**, *21*, 5734. [CrossRef] [PubMed]
7. Mazumder, P.; Khan, M.M. Design and Analysis of A Multiple Input and Multiple Output Antenna for Unmanned Aerial Vehicle. In Proceedings of the 2021 12th International Conference on Computing Communication and Networking Technologies (ICCCNT), Kharagpur, India, 6–8 July 2021; IEEE: New York, NY, USA, 2021; pp. 1–6.
8. Xiaomu, H.; Yan, S.; Vandenbosch, G.A.E. Wearable button antenna for dual-band WLAN applications with combined on and off-body radiation patterns. *IEEE Trans. Antennas Propag.* **2017**, *65*, 1384–1387.
9. Mandal, B.; Chatterjee, A.; Parui, S.K. Acrylic substrate based low profile wearable button antenna with FSS layer for WLAN and Wi-Fi applications. *Microw. Opt. Technol. Lett.* **2015**, *57*, 1033–1038.
10. Thiruvenkadam, S.; Parthasarathy, E. Compact Multiband Monopole Antenna Design for IoT Applications. *J. Electromagn. Waves Appl.* **2023**, *37*, 629–643. [CrossRef]
11. Sohel, M.; Hossain, R.; Das, D.; Paul, L.C.; Hossain, A. Design and performance evaluation of mimo antenna for uwb applications using four spanner shaped patches. In *Proceedings of the 2024 3rd International Conference on Advancement in Electrical and Electronic Engineering (ICAEEE), Gazipur, Bangladesh, 5–27 April, 2024*; IEEE: New York, NY, USA, 2024; pp. 1–6.
12. Khan, I.; Wu, Q.; Ullah, I.; Rahman, S.U.; Ullah, H.; Zhang, K. Designed circularly polarized two-port microstrip MIMO antenna for WLAN applications. *Appl. Sci.* **2022**, *12*, 1068. [CrossRef]
13. Raza, M.U.; Ren, H.; Yan, S. Dual-band monopole MIMO antenna array for UAV communication systems. *Sensors* **2024**, *24*, 5913. [CrossRef] [PubMed]
14. Zhang, C.; Tang, J.; Zhao, Y.; Jiang, Y.; Yan, M.; Zhang, L.; Tian, Q.; Xu, J. A Compact Multi-Band MIMO Antenna for UAV Communications. In *Proceedings of the 2023 International Applied Computational Electromagnetics Society Symposium (ACES-China), Hangzhou, China, 15–18 August 2023*; IEEE: New York, NY, USA, 2023; pp. 1–3.
15. Akhter, Z.; Bilal, R.M.; Shamim, A. A dual mode, thin and wideband MIMO antenna system for seamless integration on UAV. *IEEE Open J. Antennas Propag.* **2021**, *2*, 991–1000. [CrossRef]
16. Tang, H.; Bulger, C.J.; Rovere, T.; Zheng, B.; An, S.; Li, H.; Dong, Y.; Haerinia, M.; Fowler, C.; Gonya, S.; et al. A low-profile flexible dual-band antenna with quasi-isotropic radiation patterns for MIMO system on UAVs. *IEEE Antennas Wirel. Propag. Lett.* **2022**, *22*, 49–53. [CrossRef]

Disclaimer/Publisher's Note: The statements, opinions and data contained in all publications are solely those of the individual author(s) and contributor(s) and not of MDPI and/or the editor(s). MDPI and/or the editor(s) disclaim responsibility for any injury to people or property resulting from any ideas, methods, instructions or products referred to in the content.